

Tracer-cocktail injections for combined pre- and intraoperative multimodal imaging of lymph nodes in a spontaneous mouse prostate tumor model

Anne C. van Leeuwen,^{a,*} Tessa Buckle,^{a,*} Gavin Bendle,^b Lenka Vermeeren,^a Renato Valdés Olmos,^a Henk G. van de Poel,^c and Fijs W. B. van Leeuwen^a

^aAntoni van Leeuwenhoek Hospital, Division of Diagnostic Oncology, 1066 CX Amsterdam, The Netherlands

^bAntoni van Leeuwenhoek Hospital, Division of Immunology, 1066 CX Amsterdam, The Netherlands

^cAntoni van Leeuwenhoek Hospital, Netherlands Cancer Institute, Division of Surgical Oncology, 1066 CX Amsterdam, The Netherlands

Abstract. To improve surgical guidance toward prostate draining lymph nodes, we investigate the potential of intraoperative fluorescence imaging and combined pre- and intraoperative multimodality imaging approaches. Transgenic adenocarcinoma mouse prostate mice with spontaneous prostate tumors are injected intratumorally with: 1. a cocktail of patent blue (Pb) and indocyanine green (ICG); 2. a cocktail of albumin radiocolloids (^{99m}Tc-NanoColl), Pb, and ICG; or 3. a cocktail of radiolabeled albumin (^{99m}Tc-Vasculosis), Pb, and ICG. The distribution of these imaging agents over the lymph nodes (LNs) are studied at different time points after injection. We find that at 60-min postinjection, ICG significantly improves the detection of the LNs compared to Pb, 53 versus 7%, respectively. Moreover, a cocktail of ICG and ^{99m}Tc-NanoColl improves the fluorescent detection rate to 86%, equalling that of the clinically applied ^{99m}Tc-NanoColl. A similar overlap is observed in our initial clinical pilot data. Fluorescent detection of the LNs using a ICG with ^{99m}Tc-Vasculosis gives similar results as “free” ICG (58%; 60 min). A ^{99m}Tc-NanoColl, Pb, and cocktail ICG enriches the standard ^{99m}Tc-NanoColl approach by adding optical detection of the sentinel lymph nodes. Furthermore, this approach improves fluorescent-based guidance and enables both accurate surgical planning and intraoperative detection, based on a single injection. © 2011 Society of Photo-Optical Instrumentation Engineers (SPIE). [DOI: 10.1117/1.3528027]

Keywords: sentinel lymph node; surgical guidance; fluorescence; radioactivity; multimodal; albumin.

Paper 10431R received Aug. 3, 2010; revised manuscript received Nov. 5, 2010; accepted for publication Nov. 12, 2010; published online Jan. 26, 2011.

1 Introduction

The presence of metastasis in tumor draining lymph nodes (LNs) in the pelvic region is considered a strong predictor of treatment failure in patients with prostate cancer.¹ Postoperative histopathological examination of tissue samples obtained during surgery is the “golden standard” to assess the metastatic spread. To obtain these samples, extensive dissection of lymphatic tissue is required. In up to 51% of procedures, this can lead to postoperative complications such as lymphoceles, injuries to the obturator nerve and/or the ureter, and lymphedema of the lower extremity.^{2,3} Surgical pelvic lymphadenectomy procedures such as extended pelvic lymphadenectomy^{4–6} can be improved by relying on better surgical guidance toward the tumor draining lymphatic tract and LN(s). Ideally, an intraoperative imaging approach enables the surgeon to visualize and excise the tumor draining LNs accurately, which may shorten overall procedure time and decrease complication levels.

Innovations in LN mapping have originated mainly from the melanoma and breast cancer fields.^{7,8} At present, LN mapping in e.g. the breast is performed with a combination of preoperative

^{99m}Tc-labeled colloid injection and intraoperative injection of blue dyes [e.g., patent blue (Pb)] for visible guidance.⁹ In the breast, this combination method increases the detection rate from 79.6 to 93.5% for the dye alone method and ≈95% for the colloid injection to 97.7–99.2%.^{10,11}

For preoperative visualization, (static) lymphoscintigraphy at 15 min and 2 h after injection of ^{99m}Tc-labeled colloidal particles has also demonstrated its use in imaging of the tumor draining LNs in the prostate.¹² In our institute, integrated single photon emission computed tomography/computed tomography (SPECT/CT) is also used to provide superior 3-D visualization for surgical planning with a detection rate of 98%.¹³ We were not able to find any literature examples of blue-dye-based detection of the LN in the prostate. The intraoperative translation of the radiocolloid procedure requires the use of a gamma probe or camera to monitor the transit of a ^{99m}Tc-labeled colloid from the injection site into the LN, which is then dissected for histopathological examination.^{14,15} Unfortunately, the site of injection may cause a high background signal when the highly sensitive gamma probe is placed on or near the examined pelvic LNs.

As a result of its high detection sensitivity through tissues, near-infrared (NIR) fluorescence imaging is rapidly advancing in medical optical imaging.¹⁶ The excitation and emission wavelengths in the 800-nm range have better tissue penetration than

*Contributed equally to the manuscript.

Address all correspondence to: Fijs W. B. Van Leeuwen, Division of Diagnostic Oncology at the Netherlands Cancer Institute-Antoni van Leeuwenhoek Hospital, 1066 CX Amsterdam, The Netherlands. Tel: 312 051 26084; E-mail: fw.v.leeuwen@nki.nl.

the reflected blue light (400 nm) of a visible dye,¹⁷ even when much lower concentrations are used. Recently, several promising new trials have been published for breast and gastrointestinal cancer^{18,19} using the NIR fluorescent dye indocyanine green (ICG) for intraoperative fluorescence detection of LNs. Limiting factors in these studies are the effective time window, which appears to be similar to that of the visible blue dyes, and the requirement of an additional injection next to the lymphoscintigraphic approach. Accumulation of dyes in the sentinel lymph nodes (SLNs) can be achieved by using nanoparticles such as quantum dots.²⁰ However, the translation nature of such dyes is limited. In a feasibility study, the United States Food and Drug Administration (FDA) has suggested that a “cocktail” injection of fluorescent and radioactive agents would be preferable over multiple single injections.²¹ However, the same study that states this FDA suggestion also revealed that a cocktail injection of ICG with ^{99m}Tc-labeled sulfur radiocolloid reduced the fluorescence intensity by a factor of 10 and yielded poor imaging results.²² Although ^{99m}Tc-labeled sulfur colloid is the most widely used radioisotope for lymphatic mapping in the United States, in European countries ^{99m}Tc-colloidal albumin (^{99m}Tc-NanoColl) is more frequently used for identical procedures.^{22,23} We have previously demonstrated in SLN imaging using a mouse model for metastatic breast cancer (one tumor draining lymph node) that the specificity of ICG-^{99m}Tc-NanoColl complexes is similar to conventional lymphoscintigraphy.²⁴ Therefore, we reasoned that a cocktail injection of albumin (radiocolloids) and ICG could have potential.

Animal models are useful tools for investigation regarding the pathogenesis of cancers and the development of new imaging procedures.^{25,26} One of the best characterized and widely used mouse models of prostate cancer is the transgenic adenocarcinoma of the mouse prostate (TRAMP) model, which develops additional lymphatic metastasis. This tumor model provides an ideal starting point to preclinically study combined pre- and intraoperative imaging procedures in prostate cancer.

The goal of this study is to improve the accuracy of intraoperative detection of LNs for prostate cancer. Using the TRAMP model, we demonstrate that the combination of ICG and albumin in a cocktail of ^{99m}Tc-NanoColl, Pb, and ICG has great potential for combined pre- and intraoperative imaging. To further address this potential, we also show the first results of an ongoing clinical pilot study where the ICG-^{99m}Tc-NanoColl cocktail was used in six patients with prostate carcinoma.

2 Methods

2.1 Imaging Agents

Pb solutions were obtained as clinical-grade dye (Guerbet Laboratories, Birmingham, United Kingdom). ICG (Sigma Aldrich, Saint Louis, Missouri; preclinical) and ICG-pulsion (Pulsion Medical Systems AG, Irving, Texas; clinical) solution was prepared by dissolving 1.0 mg in 1.0-ml 1% Pb solution. For dye injections, 10 μ l of this solution [Pb (1.76×10^{-4} mmol); ICG (1.29×10^{-5} mmol)] was diluted in 30 μ l of a 0.9% sodium chloride solution (B. Braun, Bethlehem, Pennsylvania).

^{99m}Tc-labeled human serum albumin (^{99m}Tc-Vasculosis; 7 nm²⁵; IBA) and ^{99m}Tc-labeled colloid of human serum albumin (^{99m}Tc-NanoColl; median particle size 14 nm²⁷; GE Healthcare, Waukesha, Wisconsin) were of clinical grade and produced us-

ing standard preparation protocols. For ^{99m}Tc-Vasculosis, this means that to a clinical grade kit, a 2500-MBq (67.6 mCi) pertechnetate solution (2 ml) was added and allowed to incubate for 30 min at room temperature. For the ^{99m}Tc-NanoColl-kit, 1500-MBq (40.5 mCi) pertechnetate (2 ml) was used in combination with the same incubation procedure. The efficacy of both labeling procedures was determined via thin-layer chromatography using MeOH/water (85:15).

Cocktail injections were prepared by diluting 10 μ l of the Pb/ICG solution in 30 μ l of the respective tracer solution [^{99m}Tc-Vasculosis (1.14×10^{-6} -mmol albumin; 12 MBq or 0.32 mCi) or ^{99m}Tc-NanoColl (1.11×10^{-7} -mmol albumin; 8 MBq or 0.21 mCi)]. For the clinical procedures, cocktails were prepared under good manufacturing process (GMP) and without the presence of Pb.

To confirm the *in-situ* formation of self-assembled multimodal complexes,²⁸ protein separations were performed on the albumin particle containing cocktails in micron centrifugal filters (Millipore, Billerica, Massachusetts) with a molecular weight cut of 30,000 Da. Solutions were centrifuged for 8 min at 7×10^3 rpm and the fluorescent content of the residue and filtrate was determined.

2.2 Mice

Male TRAMP mice expressing the SV40 T antigen (TRAMP+) spontaneously develop autochthonous prostate tumors following the onset of puberty.²⁹ Lymphatic metastases occur at 24 to 28 weeks of age, and by the age of 28 weeks, 100% harbor metastatic prostate cancer in the lymph nodes or lungs.³⁰ Previous studies describe the caudal and lumbar lymph nodes as preferential sites for metastasis in orthotopic and genetically engineered mouse models for prostate cancer.^{31,32} As in the TRAMP model, the lymphatic pathway from the prostate drains via the lumbar LNs to the renal LNs. All of these LNs (see Fig. 1) were investigated for their imaging agent content. In this study, TRAMP+ mice between 25 and 30 weeks of age were used. Age-matched nontransgenic (TRAMP-) mice served as control. All animal experiments were performed in accordance with Dutch animal welfare regulations and approved by the local animal ethics committee of the Netherlands Cancer Institute–Antoni van Leeuwenhoek Hospital, Amsterdam, The Netherlands.

2.3 Injection Procedures

Animals were anesthetized with a mixture of hypnorm (Vetapharma, Leeds, United Kingdom), dormicum (Roche, Basel, Switzerland), and water [suitable for injection; 1:1:2; 5 μ l/gr intraperitoneal (i.p.)]. An incision of approximately 1 cm was made in the skin of the lower abdomen of the mice. Subsequently, mice were injected intratumorally [(i.t.); TRAMP+] or into the prostate (TRAMP-) with the respective imaging agents using a 29-G needle. The injected cocktail solutions were abbreviated as: ICG (Pb/ICG), NC (^{99m}Tc-NanoColl/Pb/ICG), and HSA (^{99m}Tc-Vasculosis/Pb/ICG). Tumorless mice were used as control and abbreviated as NC control (Table 1). This was followed by the time after injection when the LNs were dissected (e.g., 15 min) shown in subscript in Table 1.

After injection, the injection site was massaged for 5 min to stimulate lymphatic migration. With the exception of the

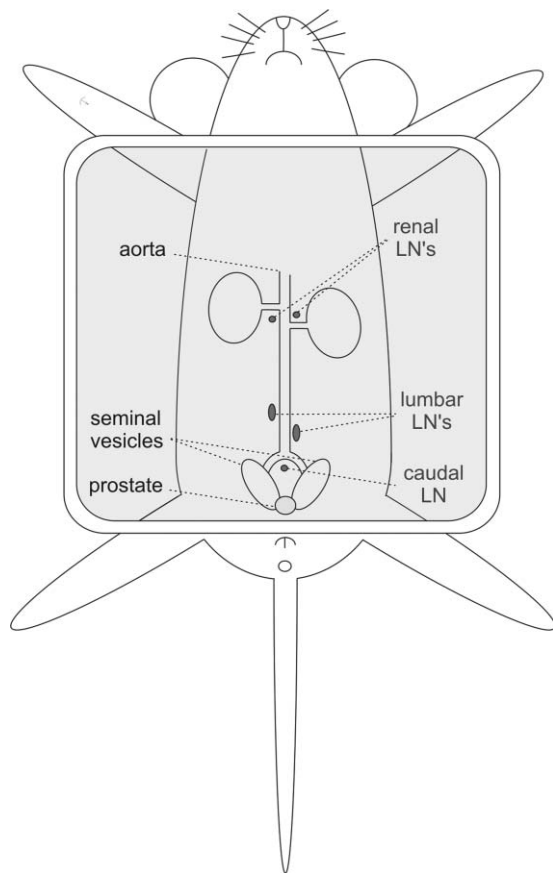


Fig. 1 Schematic representation of a mouse with an exposed abdominal cavity (in gray). Here, the five (caudal, lumbar, and renal) LNs are depicted that potentially function as the tumor draining LNs for the prostate tumors formed in the TRAMP mice.

animals that were sacrificed 15-min postinjection, the incision was closed directly after the injection and massage.

2.4 Imaging Procedures

Distribution of the imaging agents to the lymph nodes was assessed at different time points after injection (Table 1). These specific time points were chosen because they enclose a wide time window in which the pros and cons of the individual agents can be reviewed. The shortest time interval was set at 15 min after injection, as this is a standard time interval clinically used for the blue dyes. A 60-min time point was used, as previous experiments have shown that this time point is optimal for the migration of NanoColl to the SLNs of mice.²⁴ The 4-h time point was added to show that the approach is also of value at later time points.

Fluorescent and visual detection of the ICG and Pb components was conducted alone or directly following the SPECT/CT scan. After these imaging procedures, the LNs were dissected using a surgical microscope (Universal S3; Zeiss, Peabody, Massachusetts). At 15- and 60-min after injection, the LNs were evaluated visually to determine the level of blue staining. LNs were staged as not blue (0), light blue (1), or blue (2) before fluorescence imaging of the ICG component (see Table 2). In each animal, the distribution of the fluorescence and radioac-

Table 1 Different study groups and time points used for tumor draining LN imaging experiments.

Name group	Number of animals	Imaging agents used	Imaging time point (min after injection)	Detection method
ICG ₁₅	n = 6	Pb/ICG	15	Visual/ NIR fluorescence
ICG ₆₀	n = 6	Pb/ICG	60	Visual/NIR fluorescence
NC ₆₀	n = 6	NanoColl/Pb /ICG	60	SPECT/ visual/ NIR fluorescence
NC ₂₄₀	n = 6	NanoColl/Pb /ICG	240	SPECT/ visual/NIR fluorescence
HSA ₆₀	n = 6	Vasculosis/Pb /ICG	60	SPECT/ visual/ NIR fluorescence
NC ₆₀ control	n = 6	NanoColl/Pb /ICG	60	SPECT/ visual/ NIR fluorescence

tivity over the five potential tumor draining LN candidates was studied postoperatively, and the uptake values were compared to the increase in volume of the LNs (see Table 3).

2.5 Fluorescence Imaging

In-vivo fluorescence imaging was conducted on an IVIS 200 camera (Xenogen, Caliper Life Sciences, Hopkinton, Massachusetts) using Living Imaging Acquisition and Analysis software (Xenogen, Caliper Life Sciences, Hopkinton, Massachusetts). Images were acquired with standard ICG (excitation 710 to 760 nm and emission 810 to 875 nm) settings after the mice were sacrificed. For all animals, a whole body fluorescence scan was performed before dissection of the five involved LNs (see Fig. 1). To decrease background levels and increase the visibility of the LNs, the prostate and intestines were removed prior to imaging. After dissection, the lymph nodes were scanned again *ex vivo* and their fluorescent content was quantified (photons/s/cm²) using standard Living Image Analysis software and corrected for the background signal in that measurement. Because the background signal showed some small deviations, subtraction of the background signal sometimes led to negative values. As only positive fluorescent signals can be used in the experimental setup, the negative fluorescent signals were set at the minimum of zero. Trendline-based linear regression correlations (Excel) were used to establish the correlation between the fluorescence intensities and the radioactive count rate findings.

2.6 Single Photon Emission Computed Tomography/Computed Tomography

After the injection procedure, the mice were placed in a temperature-controlled (37°C) animal holder (Equipment

Table 2 Normalized fluorescent signal intensity and visibility (blue) after injection of ICG cocktails in tumor-bearing animals. Nonevaluated LNs are marked by x.

	Fluorescence intensity [Photons/s/cm ² /sr * 10 ⁶ ; background corrected]				Visibility blue dye [0; no color, 1; light blue, 2; blue]					
	Caudal	Lumbar R	Lumbar L	Renal R	Renal L	Caudal	Lumbar R	Lumbar L	Renal R	Renal L
ICG ₁₅ mouse 1	0	6	1	0	0	0	1	1	0	0
ICG ₁₅ mouse 2	5	3	4	5	0	0	1	1	0	0
ICG ₁₅ mouse 3	0	57	65	0	0	0	0	0	0	0
ICG ₁₅ mouse 4	x	1598	278	0	4	x	2	1	0	0
ICG ₁₅ mouse 5	37	453	859	173	9	2	2	2	1	0
ICG ₁₅ mouse 6	282	772	877	25	0	1	1	1	0	0
ICG ₆₀ mouse 1	1	59	66	12	0	0	0	0	0	0
ICG ₆₀ mouse 2	2	7	5	4	3	0	0	0	0	0
ICG ₆₀ mouse 3	24	461	254	x	48	1	1	1	x	1
ICG ₆₀ mouse 4	0	31	0	3	0	0	0	0	0	0
ICG ₆₀ mouse 5	0	40	0	0	4	0	0	0	0	0
ICG ₆₀ mouse 6	0	55	1	1	1	0	0	0	0	0

Table 3 Normalized fluorescent and radioactive signal intensity. Signals were measured *ex vivo*. Nonevaluated LNs were marked by **x**. In addition, the correlation between the radioactive and fluorescent signal intensities after injection of NC and HSA cocktails in TRAMP+ animals is depicted in the last column.

	Fluorescence intensity (Photons/s/cm ² /sr * 10 ⁶ ; background corrected)						Radioactive intensity (10 ³ cpm; decay corrected)						Correlation fluorescent and radioactive intensities (R ²)
	Caudal		Lumbar L		Renal R		Caudal		Lumbar R		Renal L		
NC ₆₀ mouse 1	54	18	209	4	4	0	481	142	4468	10	16	0.98	
NC ₆₀ mouse 2	49	0	2	2	2	0	3	1	1	0	0	0.92	
NC ₆₀ mouse 3	4	43	2	3	3	6	83	2927	46	57	267	1	
NC ₆₀ mouse 4	413	163	354	49	49	20	194	55	112	7	4	0.94	
NC ₆₀ mouse 5	0	40	103	0	0	0	1	226	620	2	0	1	
NC ₆₀ mouse 6	94	13	105	10	10	24	1200	469	2816	80	813	0.76	
NC ₂₄₀ mouse 1	7	19	12	15	15	5	3	243	54	55	68	0.52	
NC ₂₄₀ mouse 2	30	237	17	22	22	1	54	906	34	95	0	1	
NC ₂₄₀ mouse 3	449	105	61	0	0	5	1235	454	1317	0	167	0.41	
NC ₂₄₀ mouse 4	2	15	50	0	0	9	7	1	146	1	8	0.90	
NC ₂₄₀ mouse 5	5	15	20	0	0	4	3	5	71	1	16	0.54	
NC ₂₄₀ mouse 6	0	5	7	0	0	1	0	0	2	0	0	0.79	
HSA ₆₀ mouse 1	5	5	10	2	2	1	1	0	1	0	2	0.14	
HSA ₆₀ mouse 2	0	0	0	0	0	0	3	4	2	0	1	0.00	
HSA ₆₀ mouse 3	0	0	2	0	0	0	1	2	3	0	0	0.42	
HSA ₆₀ mouse 4	3	33	170	0	0	6	4	24	107	0	2	1	
HSA ₆₀ mouse 5	0	102	0	3	3	15	0	50	9	1	3	0.94	
HSA ₆₀ mouse 6	13	480	480	x	x	140	4	7	6	x	1	0.53	

Table 4 Normalized fluorescent and radioactive signal intensity and the correlation between the normalized radioactive and fluorescent signal intensities after injection of a NC cocktail in TRAMP-control animals.

	Fluorescence intensity (Photons/s/cm ² /sr * 10 ⁵ ; background corrected)						Radioactive intensity (10 ³ cpm; decay corrected)						Correlation fluorescent and radioactive intensities (R ²)								
	Caudal		Lumbar R		Lumbar L		Renal R		Renal L		Caudal			Lumbar R		Lumbar L		Renal R		Renal L	
NC ₆₀ control 1	5	4	20	0	0	0	8	215	396	0	0	0	0	0	0	0	0	0	0	0.80	
NC ₆₀ control 2	0	8	45	38	2	23	2	2	589	0	0	2	0	0	0	0	0	0	0	0.45	
NC ₆₀ control 3	0	6	0	0	0	0	0	25	1	1	1	51	0	0	0	0	0	0	0	0.33	
NC ₆₀ control 4	6	9	108	6	0	4	4	109	789	5	1	1	5	1	1	1	1	1	1	0.99	
NC ₆₀ control 5	82	172	54	0	10	9	9	186	8	0	0	17	0	0	0	0	0	0	0	0.78	
NC ₆₀ control 6	15	17	0	0	0	2	2	39	437	0	0	0	0	0	0	0	0	0	0	0.82	

Veterinaire Minerve, Esternay, France) before performing a SPECT/CT scan on the nano SPECT/CT (Bioscan Incorporated, Washington, D.C.), the region of interest incorporating the whole body was selected based on a (sagittal) tomographic planning x-ray image. One sequential total body SPECT scan of the same field of view was initialized, taking 30 min in total. Directly after the SPECT imaging sequence, a helical 3-D CT acquisition of the animal was performed for 12 min. After acquisition, the CT data were reconstructed with HiSPECT software (Scivis GmbH, Göttingen, Germany). The SPECT and CT datasets were automatically coregistered. The images were analyzed using the InVivoScope postprocessing software (Bioscan, Incorporated, Washington, D.C.).

2.7 Ex-Vivo Radioactivity Counting

After dissection, the amount of ^{99m}Tc in the individual lymph nodes was determined in gamma counts per minute (cpm) using a Wizard 3, 1480 automatic gamma counter (Perkin Elmer, Waltham, Massachusetts). Specimens were counted for 120 s at a 126- to 159-keV energy window, automatically including background signal measurements. For normalization, the individual radioactive count rates (^{99m}Tc) were measured and corrected for the background and radioactive decay. Correlations with the fluorescent intensity were made using the decay corrected signal intensities.

2.8 Clinical Study

During a clinical pilot study, a NanoColl-ICG cocktail was tested in six patients with prostate carcinoma. The criteria for inclusion were the presence of one or more of the following characteristics: clinical stage greater than T2b, or Gleason sum score greater than 6. The cocktail solution (240 MBq; 0.4 ml) was injected peri- and intratumorally; 0.1 ml was injected in each quadrant of the prostate. Administration was guided by transrectal ultrasonography, and each 0.1-ml injection was followed by flushing with approximately 0.7 ml of saline. During surgical pelvic lymphadenectomy, both the prostate and LNs were excised at about 60 min after injection. In all cases, the nodal areas of the interna and obturator LNs were included. Intraoperative detection of the LNs was conducted using a gamma probe. *Ex-vivo* examination of the radioactive signal in the excised LNs was detected using a portable gamma camera (Sentinella, Oncovision, Valencia, Spain). This camera is equipped with a pinhole collimator. Distribution of the radioactivity was evaluated by placing the head of the gamma camera at a distance of 5 cm above each excised specimen. Acquisition time was 1 min. Furthermore, an overview of the radioactivity within all excised nodes was made by placing the detector of the camera 10 cm above all excised nodes. Fluorescence was detected *ex vivo* using a IVIS200 scanner (see Sec. 2.3). Distribution of radioactivity was correlated to the distribution of the fluorescence; presence of radioactivity in each node was compared to the presence of fluorescence in the node. All patient studies were performed and conformed with protocol that was preapproved by the local patient ethics community of the Netherlands Cancer Institute- Antoni van Leeuwenhoek Hospital, Amsterdam, The Netherlands, and were carried out after patient consent.

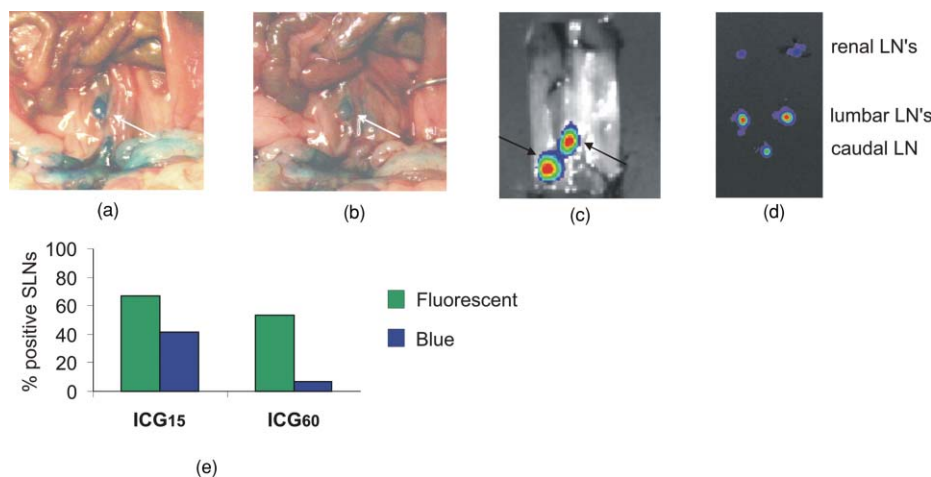


Fig. 2 Imaging of the sentinel node with visible Pb and NIR fluorescent ICG. (a) Intraoperative detection of Pb in the right lumbar LN, directly after massage of the injection site and (b) after 15 min, showing the washout of the dye during this time period. (c) Intraoperative NIR fluorescence imaging of the lumbar LNs with “free” ICG, which was visible up to 60 min after injection. (d) The fluorescent content can be detected and quantified in excised LNs. (e) Percentages of imaging agents containing (positive) LNs in the ICG₁₅ and ICG₆₀ groups. In the graphs, the percentages of the fluorescent component in the cocktail are depicted in green and the percentages for the visible component in blue; percentages are calculated from Table 2.

3 Results

3.1 Lymphatic Migration Studies

The lymphatic migration toward the tumor draining LNs was studied with visible, fluorescent, and radioactive imaging agents. Similar to a clinical situation,³¹ we observed that the lymphatic migration of the imaging agents from the injection site is greatly improved by a massage (5 min) of the injection site, whereas almost no drainage could be detected when no massage was applied (data not shown). This was especially important for the 15- and 60-min groups. In these groups the animals remained anesthetized until imaging, limiting the spontaneous massage by movement. In the 240-min groups, the animals awoke from their initial anesthetics, and animals were able to walk around freely in the cage (hereby also spontaneously massaging the prostate).

As lymphatic migration depends on the injection site and may vary between individual animals, the measured signal intensities (see Tables 2, 3, and 4) show some fluctuations within the different groups. The radioactive count rates obtained with ^{99m}Tc-NanoColl tend to vary (Tables 3 and 4), which can, in part, also be attributed to a variation in particle sizes, as a single ^{99m}Tc-NanoColl preparation consists of a wide range of particle sizes with a median of 14 nm. In different ^{99m}Tc-NanoColl batches, however, the distribution of particle sizes may vary.

3.2 Distribution of Patent Blue/Indocyanine Green

To create an imaging approach that would allow both visible and NIR fluorescent detection, a cocktail of Pb and ICG was prepared (defined as ICG-cocktail; see Table 1). The distribution of the visual substance of the cocktail Pb was first assessed. When massage of the injection site was performed after injection, lymph nodes stained blue and the lymphatic tract became visible. At 15- and 60-min postinjection, the visible blue nodes stained a lower grade of blue than observed directly after massage (the first 5-min postinjection), indicating a quick wash-out of Pb [Figs. 2a and 2b; Table 2]. The visible blue dye could best be observed in LNs in the ICG₁₅ group, where Pb uptake could be seen

in at least two LNs in five of the six animals. However, only 42% of all the excised LNs showed blue staining. After 60 min, the detection efficacy was reduced even further to 7% [see Fig. 2e].

Within the ICG groups, all “blue” LNs were fluorescent. Overall, the fluorescent intensities in the ICG₆₀ group are lower compared to those in the ICG₁₅ group (see Table 2). The ability to specifically detect the LNs using the fluorescent ICG signal also decreases in time. After 15 min, 67% of the LNs could be detected, whereas after 60 min, this was only 53%.

Even though the initial concentration of ICG that is injected is 14 times lower than that of Pb, fluorescence detection of ICG enables a much longer functional imaging time period postinjection. Multiple LNs are fluorescent with a variety of intensities. In ten out of twelve animals, the maximal fluorescence intensity was measured in one or both of the lumbar LNs (Table 2).

3.3 Combined Single Photon Emission Computed Tomography and Fluorescence Imaging

Radiotracer experiments (using ^{99m}Tc-NanoColl or ^{99m}Tc-Vasculosis) were performed with cocktail solutions that also contain Pb and ICG. Separation of the albumin from the cocktail with a size exclusion filter revealed that while no ICG had passed the filter, Pb was present in the filtrate. In the presence of a 14-fold excess of Pb, all the ICG had formed a complex with albumin via self-assembly. Since this self-assembled binding cannot be established in a covalent manner, this complex formation is based on noncovalent interactions caused by the charges and lipophilic groups on ICG and albumin.³⁴ In this cocktail, this binding is unique to ICG, as we could not observe any binding of Pb to the albumin (colloids). If a small amount of binding between Pb and the albumin did occur, it was not enough to aid in visual detection of the LNs. Hence in the cocktail injections, a multimodal complex is present that comprises a radioactive (^{99m}Tc-Vasculosis or ^{99m}Tc-NanoColl) and a fluorescent (ICG) component. Based on the results with the ICG cocktails (see previous), it can be concluded that after 60 min or more, the “free” Pb component in this NC cocktail only enables

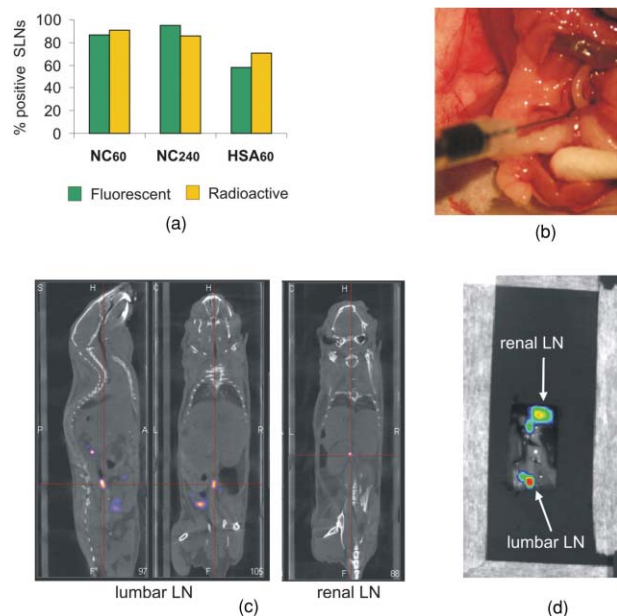


Fig. 3 NC₆₀ cocktail-based imaging of the tumor draining LNs. (a) Percentages of imaging agents containing LNs in the ICG₁₅ and ICG₆₀ groups. In the graphs, the percentages of the fluorescent component in the cocktail are depicted in green and the percentages for the radioactive component in yellow; percentages are calculated from Table 3. (b) Visualization of the injection accuracy via the visible Pb component. (c) Preoperative SPECT/CT imaging via the radioactive NanoColl component, depicting a.o. a lumbar and a renal LN. (d) Intraoperative NIR fluorescence imaging of the fluorescent ICG component animal revealing only lumbar and renal LNs. To minimize the background signal, except for the ROI the animal was covered.

the identification of the injection accuracy (e.g., leakage of the injected volume out of the injection site), which is not possible with nondye containing radiopharmaceutical injections.

Preoperative SPECT/CT imaging using a dedicated small-animal SPECT/CT system makes it possible to mimic the standard preoperative clinical lymphoscintigraphy-based assessment in mice. The NC or HSA cocktail was injected and SPECT/CT images were made at 60- or 240-min postinjection. Next to lymphatic migration, the injected radiopharmaceuticals also showed distribution throughout the tumor and seminal vesicles. In combination with the relatively small migratory distances and the 1-mm SPECT resolution, the preclinical SPECT/CT scans only allowed for the preoperative determination of uptake in the lumbar and renal LNs. Therefore, to quantitatively study the radioactive content in all five lymph nodes, postoperative scintillation counting was used. This predominantly revealed the highest uptake values in either the caudal and/or lumbar LNs (see Table 3).

Within the NC₆₀ group, the radioactive and fluorescent signal intensities had very good correlation (Table 3); five out of six animals gave a correlation of $R^2 \geq 0.92$. Nonetheless, the remaining animal presented a R^2 value of 0.76 (mouse 6). Mouse 2 within this group reported very low radioactive signals within all LNs compared to the other animals in this group. However, this did not have a negative influence on the correlation of the radioactive and fluorescent signal intensities. On average, the fluorescent intensities were higher than those with ICG alone at 60 min. Furthermore, in four out of six animals all the LNs

could be identified based on both their radioactive and fluorescent signatures. Of all the LNs in this group, 86 and 91% are respectively fluorescent or radioactive. [see Fig. 3(a)].

To study the effective time window and provide an indication of the stability of the cocktail approach, we also investigated the LN uptake at 240-min postinjection (NC₂₄₀, Table 3). Other than in the NC₆₀ group, only three out of six animals showed a good correlation between the radioactive and fluorescent signal intensities ($R^2 \geq 0.79$). In all of the NC₂₄₀ animals, the LN with the highest radioactive content was also fluorescent, and in five out of six animals, all of the LNs were fluorescent and had radioactive content (only three out of six had a radioactive content above 10^3 cpm). 95% of the LNs in this group were fluorescent and 86% were radioactive [see Fig. 3a].

Within the HSA₆₀ group, noticeably lower average signal intensities were measured compared to the NC₆₀ group. Furthermore, the correlation between the normalized radioactive and fluorescent intensities in these animals was quite poor, as only two out of six mice gave a good correlation ($R^2 \geq 0.78$). In only two out of six animals, all LNs were fluorescent and had a radioactive content (content mouse 1 was below 10^3 cpm). Furthermore, only 58 and 71% of all LNs were respectively fluorescent or radioactive. As can be seen in Fig. 3(a), the correlation between the percentage of LNs that were fluorescent and the LNs that were radioactive in the NC group was high at 60 min after injection. This correlation remained high at 240 min after injection. Therefore, this complex can be considered stable over the time period measured.

3.4 Preliminary Clinical Data

The concept of using the NC cocktails (no PB present) in clinical procedures involving the excision of both the prostate and the nearby LNs is currently under investigation. Here we only report on the initial *ex-vivo* results ($n = 6$) to substantiate the translational nature of the presented preclinical data. Patients were injected with the cocktail solution in the operating theater, and the prostate and LNs were excised approximately 60 min after injection, hence mimicking the preclinical NC₆₀ conditions. Examination of the excised tissue sections (see LNs in Fig. 4) demonstrates the overlap between the fluorescent and radioactive signals. All fluorescent LNs contained radioactivity and vice versa. Although this is preliminary data, the results indicate that the approach is also of value in patients.

4 Discussion

In the clinic it is important to identify the first LN or group of LNs reached by metastasizing cancer cells via lymph flow. As it has been shown that lymph flow increases in tumor-bearing animals,³⁵ our experiments were conducted in TRAMP+ mice that develop spontaneous tumors in the prostate accompanied by metastatic spread.³³ Although in the TRAMP model, the prostate-dependent drainage pathways resemble the clinical situation, the lymphatic drainage pattern differs slightly from that seen in patients. Lymphatic drainage logically occurs via the caudal and lumbar LNs to the renal LNs, and can occur via LN in either the left or right drainage path. Hence the described approach also appears to be able to visualize secondary LNs.

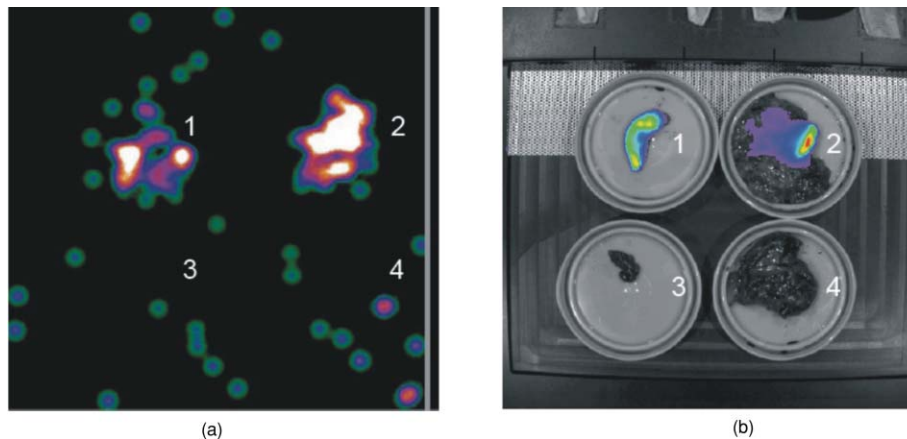


Fig. 4 *Ex-vivo* analysis of excised LNs. LNs situated in the extended pelvic lymphadenectomy area (LN 1 through 4) were excised during a laposcopic procedure, approximately 60 min after the cocktail solution was injected into the prostate. *Ex-vivo* evaluation of the excised tissue using a gamma camera (a) showed a radioactive signal in two of the four excised nodes. Fluorescent imaging (b) resulted in visualization of a fluorescent signal in the same nodes where the radioactive signal could be detected.

Histological evaluation of lymphatic tissue after surgical pelvic lymphadenectomy procedures is acknowledged as the gold standard in the assessment of lymph node metastasis in the field of prostate cancer. To simplify the excision of these LNs, accurate surgical guidance is crucial. Unfortunately, very little intraoperative imaging techniques are reported for this cancer type, and techniques for multimodal pre- and intraoperative visualization of the tumor draining LNs are lacking. The TRAMP model for metastatic prostate cancer serves as a good mouse model for the development and validation of new (intraoperative) lymph node imaging procedures based on cocktail injections of Pb, ICG, ^{99m}Tc -Vasculosis, and/or ^{99m}Tc -NanoColl.

4.1 Visual (Patent Blue) Versus Fluorescence (Indocyanine Green) Detection

Pb and ICG show chemical similarities; both contain aromatic units with a cationic nitrogen atom and two anionic groups for water solubility. As a result, a similar lymphatic migration and thus a similar effective time window were foreseen. Unexpectedly, no direct correlation could be observed between the detection of Pb and ICG (see Table 2). Visible blue dye guided dissection would, in the ICG₁₅ group, only result in the removal of 42% of all LNs of interest, while via fluorescent detection, this percentage improves to 67%. Moreover, at 60 min after injection, the fluorescent dye still enables visualization of 53% of the LNs compared to only 7% with Pb. Since both imaging agents are injected as a cocktail, an explanation for the differences in identification of LNs could be the higher detection sensitivity obtained with the NIR dye ICG. This improved sensitivity is especially interesting, considering that the Pb/ICG cocktails contain Pb in a 14-fold excess with respect to ICG. As a result of the poor visualization rate, Pb was eliminated from the clinical cocktail, as surgery was initiated at approximately 60-min postinjection. At this time, it was not expected that Pb would positively effect the detection rate intraoperatively. It must be noted that the validation of the accuracy of the injection could therefore not be done visually.

4.2 Diagnostic Value of Radioactive Albumin (Colloid) Containing Cocktail Injections

Preoperative SPECT/CT with radiocolloids is a reliable method to detect the tumor draining LNs of the prostate, and by doing so it helps plan the surgical procedure and reduces operating time.³⁶ With NC and HSA cocktail injections, the radioactive component can be used for surgical planning (preoperative SPECT/CT). The other two components complement this clinically proven technique by adding the possibility to: 1. validate the accuracy of the injection site using the Pb component, and 2. guide the surgical procedure by intraoperative NIR fluorescence imaging (Fig. 3). As a result, the cocktail approach combines the advantages of three different detection procedures in one injection.

Lymphatic migration studies using differently sized imaging agents have led to questions regarding the optimal particle size for optimal migration in the lymphatic tract. Fujii, Kitagawa, and Kumbo³⁷ showed that molecules with a hydrodynamic diameter less than approximately 10 nm (namely Pb, ICG, and ^{99m}Tc -Vasculosis) have the potential to travel beyond the tumor draining LN, while larger molecules <100 nm diam (namely ^{99m}Tc -NanoColl) are retained in the tumor draining LN. Furthermore, Faries et al.³⁸ demonstrated that albumin colloids are actively accumulated by macrophages in the LNs. Indeed, we find that at 60- and 240-min postinjection, the radioactive count rates obtained with the albumin colloids (^{99m}Tc -NanoColl) on average are higher than those obtained with single albumin particles (^{99m}Tc -Vasculosis; see values Table 3).

Crucial for combined pre- and intraoperative visualization of the multimodal nature of the approach is the ability to identify all LNs based on both their radioactive and fluorescent contents. Not only is there a high correlation between the fluorescent signal intensities and radioactive count rates in the NC groups (Tables 3 and 4), both modalities also show highly similar percentages of detected LNs, 86 and 95%, respectively [Fig. 3a]. The latter underlines the high sensitivity of the radiocolloid approach. The overall fluorescent intensities in the NC₆₀ group are highly similar to those obtained with “free” ICG at 60 min (see Tables 2, 3, and 4), suggesting that the interaction with albumin

does not have a negative influence on the fluorescent emission. Moreover, the ability to detect the LNs via fluorescence imaging in the NC₆₀ group increases by 33% compared to that with “free” ICG. The multimodal HSA cocktail, on the other hand, does not give an improvement in fluorescence detection of LNs compared to the “free” ICG at 60-min postinjection, respectively 58 and 53% [see Figs. 2e and 3a]. Combined, the high similarity in fluorescence distribution and the low correlation between fluorescent signal intensities and radioactive count rates found for the HSA cocktail suggest that the complex stability in the latter is lower than in the NC cocktails.

While all animals in the NC₆₀ group have a correlation ≥ 0.76 , only three animals in the HSA₆₀ group give such a correlation. Based on the molar ratios used in the cocktails, the ICG: ^{99m}Tc-Vasculosis (HSA) ratio is much lower than with NC. Clearly, the multimodal nature of the noncovalent complexes that formed ^{99m}Tc-NanoColl is less influenced by dissociation of ICG compared to the complexes formed with HSA (see Table 3). At a later time point (NC₂₄₀) dissociation of ICG from ^{99m}Tc-NanoColl also becomes detectable; only three animals give a correlation ≥ 0.79 . In the NC₂₄₀ group, LNs are also present that are fluorescent but not radioactive (see Table 3). This indicates that in these instances, ICG dissociates from ^{99m}Tc-NanoColl and is separately distributed over the LNs.

Even though the fluorescent and radioactive signals for NC₂₄₀ and HSA₆₀ are not all correlated at the quantitative level, it is still possible to also see the radioactive LNs via NIR fluorescence imaging procedures. As long as some of the ICG remains bound to the radioactive albumin particles, the LNs can be detected via fluorescence imaging. In these instances, the self-assembled systems can still help guide the surgical resection via intraoperative NIR imaging.

With the NC₆₀ control group, a slightly lower correlation between the fluorescent and radioactive signal was found in TRAMP animals that were injected in the prostate (see Table 3). It seems that the self-assembled complexes are less stable after injection in the highly vascularised prostate. This agrees with our findings (data not shown) that these self-assembled systems are not stable in the blood stream after intravenous injection. The efficacy of the self-assembled complexes in intratumoral injections, however, is an indication that the physiology in the tumor is favorable for complex stability. Combined, this suggests that the physiological conditions of the injection site are of influence on the stability of the noncovalent self-assembled complexes. Nevertheless, it warrants their use in intratumoral injections and lymphatic migration studies.

4.3 Clinical Applicability

Because the local Netherlands Cancer Institute ethical committee also acknowledges that a single cocktail injection of fluorescent and radioactive agents would be preferable over multiple injections (see Sec. 1), the use of ICG and ^{99m}Tc-NanoColl containing cocktail injections was approved in a clinical pilot study. Different, of course, from the United States, is the local use of albumin radiocolloids, rather than sulphur radiocolloids.²¹ We have shown that this combination yields the *in-situ* formation of a noncovalent complex comprising two clinically approved imaging agents. Hence, different from what was found with

sulphur radioaccolloids, here a cocktail injection provides clear added value over “free” ICG alone.

At this point, we only have shown *ex-vivo* validation data to demonstrate the excellent correlation between the radioactive and fluorescent signal in a select amount of patients. Further studies will be conducted using an intraoperative fluorescence camera, allowing intraoperative visualization of the nodes during the surgical procedure. The preliminary clinical data are promising and substantiate the potential the approach might have in a clinical application. Currently, we are further investigating the clinical value of this approach. The presented preclinical data/knowhow acts as guideline.

5 Conclusions

On top of conventional preoperative SPECT/CT guidance, LN imaging with a cocktail solution of Pb, ICG, and ^{99m}Tc-NanoColl gives additional visual information regarding the accuracy of the injection (Pb), and provides the possibility of optical fluorescence guidance during the surgical procedure (ICG). Due to the self-assembly of ICG and ^{99m}Tc-NanoColl, a multimodal complex is generated that enables both pre- and intraoperative detection of the LNs up to 240-min postinjection. This approach is currently used in clinical trials, where to what extent the cocktail approach adds an extra dimension to the already applied radiocolloid procedure is being investigated.

Acknowledgments

This research is supported by the Technology Foundation, applied science division of now, and the technology program of the Ministry of Economic Affairs (STW BGT 7528 Veni). We thank Bert Pool and the technical staff of the Department of Nuclear Medicine at the NKI-AVL for their support, and Patrick Chin and Chantal Beekman for critically reviewing the manuscript.

References

1. M. Fujisawa and H. Miyake, “Significance of micrometastases in prostate cancer,” *Surg. Oncol.* **154**, 247–252 (2008).
2. A. Heidenreich, C. H. Ohlmann, and S. Polyakov, “Anatomical extent of pelvic lymphadenectomy in patients undergoing radical prostatectomy,” *Eur. Urol.* **52**, 29–37 (2007).
3. A. Briganti, F. K. H. Chun, A. Salonia, N. Suardi, A. Gallina, L. F. Da Pozzo, M. Roscigno, G. Zanni, L. Valiquette, P. Rigatti, F. Montorsi, and P. I. Karakiewicz, “Complications and other surgical outcomes associated with extended pelvic lymphadenectomy in men with localized prostate cancer,” *Eur. Urol.* **50**, 1006–1013 (2006).
4. R. E. Link and R. A. Morton, “Indications for pelvic lymphadenectomy in prostate cancer,” *Urol. Clin. North. Am.* **28**, 491–498 (2001).
5. B. A. Wilkinson and F. C. Hamdy, “State-of-the-art staging in prostate cancer,” *BJU Int.* **87**, 423–431 (2001).
6. P. Bader, F. C. Bukhard, R. Markwalder, and U. E. Studer, “Is a limited lymph node dissection an adequate staging procedure for prostate cancer?” *J. Urol.* **168**, 514–518 (2002).
7. A. E. Giuliano, D. M. Kirgan, J. M. Guenther, and D. L. Morton, “Lymphatic mapping and sentinel lymphadenectomy for breast cancer,” *Ann. Surg.* **220**, 391–398 (1994).
8. D. L. Morton, J. F. Thompson, A. J. Cochran, N. Mozzillo, R. Elashoff, R. Essner, O. E. Nieweg, D. F. Roses, H. J. Hoekstra, C. P. Karakousis, D. S. Reintgen, B. J. Coventry, E. C. Glass, and H. J. Wang, “Sentinel node biopsy or nodal observation in melanoma,” *N. Engl. J. Med.* **355**, 1307–1317 (2006).
9. G. Mariani, P. Erba, G. Villa, M. Gipponi, G. Manca, G. Boni, F. Buffoni, F. Castagnola, G. Paganelli, and H. W. Strauss, “Lymphoscintigraphic and intraoperative detection of the sentinel lymph

- node in breast cancer patients: the nuclear medicine perspective," *J. Surg. Oncol.* **85**, 112–122 (2004).
10. E. Pelosi, A. Ala, M. Bellò, A. Douroukas, G. Migliaretti, E. Berardengo, T. Varetto, R. Bussone, and G. Bisi, "Impact of axillary nodal metastasis on lymphatic mapping and sentinel lymph node identification rates in patients with early stage breast cancer," *Eur. J. Nucl. Med. Biol. Imag.* **32**, 937–942 (2005).
 11. T. Hayashida, H. Jinno, M. Sakata, M. Takahashi, T. Onishi, H. Seki, T. Sato, T. Nakahara, N. Shigematsu, M. Mukai, T. Hibi, M. Kitajima, and Y. Kitagawa, "Superiority of radioisotope over blue dye for sentinel lymph node detection in breast cancer," *Eur. Surg. Res.* **44**, 111–116 (2010).
 12. S. H. Warncke, A. Mattei, F. G. Fuechsel, S. Z'Burn, T. Krause, and U. E. Studer, "Detection rate and operating time required for γ probe-guided sentinel lymph node resection after injection of Technetium-99m nanocolloid into the prostate with and without preoperative imaging," *Eur. Urol.* **52**, 126–133 (2007).
 13. L. Vermeeren, R. A. Valdés Olmos, W. Meinhardt, A. Bex, H. G. van der Poel, W. V. Vogel, F. Sivo, C. A. Hoefnagel, and S. Horenblas, "Value of SPECT/CT for detection and anatomic localization of sentinel lymph nodes before laproscopic sentinel node lymphadenectomy in prostate carcinoma," *J. Nucl. Med.* **50**, 865–870 (2009).
 14. W. Meinhardt, R. A. Valdés Olmos, H. G. van der Poel, A. Bex, and S. Horenblas, "Laparoscopic sentinel node dissection for prostate carcinoma: technical and anatomical observations," *BJU Int.* **102**, 714–717 (2008).
 15. R. A. Valdes Olmos, S. Vidal-Sicart, and O. E. Nieweg, "SPECT-CT and real-time intraoperative imaging: new tools for sentinel node localization and radioguided surgery?" *Eur. J. Nucl. Med Mol. Imag.* **36**, 1–5 (2009)
 16. J. V. Frangioni, "In vivo near-infrared fluorescence imaging," *Curr. Op. Chem. Biol.* **7**, 626–634 (2003)
 17. Y. T. Lim, S. Kim, A. Nakayama, N. E. Stott, M. G. Bawendi, and J. V. Frangioni, "Selection of quantum dot wavelengths for biomedical assays and imaging," *Mol. Imag.* **2**, 50–64 (2003).
 18. Y. Ogasawara, H. Ikeda, M. Takahashi, K. Kawasaki, and H. Doihara, "Evaluation of breast lymphatic pathways with indocyanine green fluorescence imaging in patients with breast cancer," *World J. Surg.* **32**, 1924–1929 (2008).
 19. M. Kusano, Y. Tajima, K. Yamazaki, M. Kato, M. Watanabe, and M. Miwa, "Sentinel node mapping guided by indocyanine green fluorescence imaging: a new method for sentinel node navigation surgery in gastrointestinal cancer," *Dig. Surg.* **25**, 103–108 (2008).
 20. P. T. K. Chin, T. Buckle, A. Aguirre de Miguel, S. C. J. Meskers, R. A. J. Janssen, and F. W. B. van Leeuwen, "Dual emissive quantum dots for multispectral intraoperative fluorescence imaging," *Biomaterials* **31**, 6823–6832 (2010).
 21. E. M. Sevick-Muraca, R. Sharma, J. C. Rasmussen, M. V. Marshall, J. A. Wendt, H. Q. Pham, E. Bonifas, J. P. Houston, L. Sampath, K. E. Adams, D. K. Blanchard, R. E. Fisher, S. B. Chiang, R. Elledge, and M. E. Mawad, "Imaging of lymph flow in breast cancer patients after microdose administration of a near-infrared fluorophore," *Radiol.* **246**, 734–741 (2008).
 22. E. A. Newman and L. A. Newman, "Lymphatic mapping techniques and sentinel lymph node biopsy in breast cancer," *Surg. Clin. North Am.* **87**, 353–364 (2007).
 23. L. A. Newman, "Lymphatic mapping and sentinel lymph node biopsy in breast cancer patients: a comprehensive review of variations in performance and technique," *J. Am. Coll. Surg.* **199**, 804–816 (2004).
 24. T. Buckle, A. C. van Leeuwen, P. T. K. Chin, H. Janssen, S. Muller, J. Jonkers, and F. W. B. van Leeuwen, "A self-assembled multimodal complex for combined pre- and intraoperative imaging of the sentinel lymph node," *Nanotechnol.* **21**, 355101 (2010).
 25. R. Weissleder, "Scaling down imaging: molecular mapping of cancer in mice," *Nature Rev. Cancer* **2**, 11–8 (2002).
 26. S. F. Winter, A. B. Cooper, and N. M. Greenberg, "Models of metastatic prostate cancer: a transgenic perspective," *Prostate Cancer Prostatic Dis.* **6**, 204–211 (2003).
 27. S. Ohnishi, S. J. Lomnes, R. G. Laurence, A. Gogbashian, G. Mariani, and J. V. Frangioni, "Organic alternatives for quantum dots for intraoperative near-infrared fluorescent sentinel lymph node mapping," *Mol. Imag.* **4**, 172–181 (2005).
 28. E. D. Moody, P. J. Viskari, and C. L. Colyer, "Non-covalent labeling of human serum albumin with indocyanine green: a study by capillary electrophoresis with diode laser-induced fluorescence detection," *J. Chrom. B* **729**, 55–64 (1999).
 29. A. A. Hurwitz, B. A. Foster, J. P. Allison, N. M. Greenberg, and E. D. Kwon, "The TRAMP mouse as a model for prostate cancer," *Curr. Protoc. Immunol.* Chapter 20, unit 20.5 (2001).
 30. S. Gupta, N. Ahmad, S. R. Marengo, G. T. MacLennan, N. M. Greenberg, and H. Mukhtar, "Chemoprevention of prostate carcinogenesis by alpha-difluoromethylornithine in TRAMP mice," *Cancer Res.* **60**, 5125–5133 (2000).
 31. N. Rubio, M. M. Villacampa, N. El Hilali, and J. Blanco, "Metastatic burden in nude mice organs measured using prostate tumor PC-3 cells expressing the luciferase gene as quantifiable tumor cell marker," *Prostate* **44**, 133–143 (2002).
 32. S. B. Shappell, G. V. Thomas, R. L. Roberts, R. Herbert, M. M. Ittmann, M. A. Rubin, P. A. Humphrey, J. P. Sundberg, N. Rozengurt, R. Barrios, J. M. Ward, and R. D. Cardiff, "Prostate pathology of genetically engineered mice: definitions and classification. The consensus report from the bar harbor meeting of the mouse models of human cancer consortium prostate pathology committee," *Cancer Res.* **64**, 2270–2305 (2004).
 33. S. S. Bass, C. E. Cox, C. J. Salud, G. H. Lyman, C. McCann, E. Dupont, C. Berman, and D. S. Reintgen, "The effects of postinjection massage on the sensitivity of lymphatic mapping in breast cancer," *J. Am. Coll. Surg.* **192**, 9–16 (2001).
 34. U. Kragh-Hansen, "Molecular aspects of ligand binding to serum albumin," *Pharm. Rev.* **33**, 17–53 (1981).
 35. A. Ruddell, M. I. Harrell, S. Minoshima, B. M. Iritani, S. W. White, and S.C. Partridge, "Dynamic contrast-enhanced magnetic resonance imaging of tumor-induced lymph flow," *Neoplasia* **10**, 706–713 (2007).
 36. U. E. Studer, "Detection rate and operating time required for gamma probe-guided sentinel lymph node resection after injection of technetium-99m nanocolloid into the prostate with and without preoperative imaging," *Eur. Urol.* **52**, 126–32 (2007).
 37. H. Fujil, Y. Kitagawa, and A. Kumbo, "Sentinel nodes of malignancies originating in the alimentary tract," *Ann. Nucl. Med.* **18**, 1–12 (2004).
 38. M. B. Faries, I. Bedrosian, C. Reynolds, H. Q. Nguyen, A. Alavi, and B. J. Czerniecki, "Active macromolecule uptake by lymph node antigen-presenting cells: a novel mechanism in determining sentinel lymph node status," *Ann. Surg. Onc.* **7**, 98–105 (2000).